Electronic Supplementary Material (ESI) for Energy & Environmental Science.
This journal is © The Royal Society of Chemistry 2017

Electronic Supplementary Information (ESI) for

A general polymer-assisted strategy enables unexpected efficient metal-free oxygen-evolution catalysis on pure carbon nanotubes

You Zhang,[a,§] Xuliang Fan,[a,§] Junhua Jian,[a,§] Dingshan Yu,[a,*] Zishou Zhang, [a,*] and Liming Dai [b,*]

[a] Y. Zhang,[§] X. L. Fan,[§] J. H. Jian,[§] Prof. D. S. Yu,[*] Prof. Z. S. Zhang,[*]
key Laboratory for Polymeric Composite and Functional Materials of Ministry of Education,
Key Laboratory of High Performance Polymer-based Composites of Guangdong Province,
School of Chemistry Sun Yat-Sen University, Guangzhou, 510275, China.
E-mail: yudings@mail.sysu.edu.cn, zhzish@mail.sysu.edu.cn

[b] Prof. L. M. Dai[*]
Department of Macromolecule Science and Engineering, Case Western Reserve University,
Cleveland, OH 44106, USA.
E-mail: liming.dai@case.edu

Materials

All reagents and chemicals were from commercially sources. Poly(ethylene-alt-maleic anhydride) (PEM, average M_w 100000-500000), Poly(ethylene glycol) (PEG, average M_w 600000) and Poly(vinyl acetate) (PVAc, average M_w 500000) were purchased from Sigma-Aldrich Co. Poly(vinyl alcohol) (PVA, alcoholysis 87.0-89.0%) and Poly(acrylic acid) (PAA, average M_w 4000000) were purchased from Aladdin Co. Poly (ethylene-alt-maleic acid) (PEMAc) is the hydrolysate of poly(ethylene-alt-maleic anhydride) (PEM).

Preparation of Free-standing Polymer@CNT Composite Membranes

To minimize the possible damage of the conjugated structure of carbon nanotubes (CNTs) surface, CNTs from (Nanocyl NC 7000) were purified by refluxing in 6 mol/L hydrochloric acid for overnight, instead of concentrated nitric or sulfuric acid. Herein, it is noted that the CNT is only purified by non-destructive HCl treatment without any oxidative process. This treatment avoids the introduction of surface oxygen groups on CNTs, supported by many previous reports[S1-S4] and our XPS results (Fig. S1). The flexible composite membranes were prepared through a simple solution-cast method as described below: Firstly, a predetermined amount of polymer was dissolved in 25 mL of appropriate solvent (acetone/water for PEMAc; deionized water for other polymer in our present work) by stirring for 30 min with a magnetic stirrer (IKA Color Squid). Thereafter, 0.1 g of pure CNTs were uniformly dispersed in the polymer solution with the assistance of sonication in an ice bath. Here, by varying the polymer mass, the mass ratios of the polymer to CNTs were 10: 90 or 20: 80 or 5: 95. Herein, a high frequency, low power sonic bath (Elmasonics, 40 kHz) was used for sonication in order to reduce the sonication effect on the polymer and nanotubes. After sonicating for 20 min, the resulting CNT@polymer dispersion was poured into a vessel (glass surface dish). Finally, the composite membrane was obtained after the complete evaporation of the solvent, followed by mechanically peeling. It should be pointed out that PEM was used for the synthesis for PEMAc@CNTs membranes. PEM and CNTs were dispersed in the acetone/water mixture with sonication, which led to the hydrolysis of PEM into PEMAc. The final product was thus PEMAc@CNTs membranes. This structure changes could be monitored by infrared spectroscopy. The pure PEM exhibited obvious anhydride signals at 1782 and 1858 cm^{-1}. In contrast, for the obtained final product, the anhydride signals disappeared completely and new signals at 1376 and 1462 cm^{-1} appeared corresponding to the symmetrical and antisymmetrical of carboxylic anions, confirming the formation of PEMAc@CNTs. The obtained samples were denoted as PEMAc@CNTs90, PEMAc@CNTs95, PEMAc@CNTs80, PAA@CNTs90, PVA@CNTs90, PVAc@CNTs90, and PEG@CNTs90.

As a control experiment, pure CNT membrane was also prepared by the similar method. In brief, an appropriate amount (0. 1g) of pure CNTs were uniformly dispersed in 25 mL acetone with the assistance of sonication in an ice bath. Herein, a high frequency, low power sonic bath (Elmasonics, 40 kHz) was used for sonication. After sonicating for 20 min, the resulting CNT dispersion was poured into a vessel (glass surface dish). Finally, the pure CNT membrane was obtained after the complete evaporation of the solvent, followed by mechanically peeling.

Material Characterization

The morphology and microstructure were characterized by using scanning electron microscopy (SEM; Hitachi S-4800, Japan) with cold field emission gun working at 10.0 kV acceleration voltage and transmission electron microscopy (TEM; JEM-2100F, Japan), high-resolution TEM (HRTEM, 200 kV). The XPS spectra were measured using an ESCA Lab250 X-ray photoelectron spectrometer. All XPS spectra were corrected using the C1s line at 284.8 eV, along with curve fitting and background subtraction. The XPS spectra were referenced to C1s emission at 284.8 eV and fitted by Gauss type and the FWHM was constrained to < 3 eV while the Lorentzian-Gaussian constant was all set as 20%. Raman spectra were recorded on a Renishaw Raman system model 1000 spectrometer with a 20 mW air-cooled argon ion laser (514.5 nm) as the excitation source. The inductively coupled plasma mass spectra (ICP-MS) of CNTs samples were recorded on a ThermoFisher Scientific Icap Qc Quadrupole ICP-MS. The water contact angles (θ) of the samples were measured by using a Kruss DSA100 analysis system at ambient temperature. Brunauer-Emmett-Teller (BET) surface area was measured from N_2 adsorption and desorption isotherms by an ASAP 2460 system at 77 K. The conductivities of pure CNT membrane and PEMAc@CNT90 were measured to be about 43 ± 1 and 41 ± 1 S/cm, respectively, by a standard four-probe method using a ST2253 testing system. Clearly, the polymer@CNT90 membrane still exhibits good conductivity without obvious decrease relative to that of the pure CNT membrane, indicating that ultrathin polymer coating on the nanotube surface (Figure 1 in the main text) in the polymer@CNT90 (90 wt% CNT) membrane causes little effect on charge transfer of the composite electrodes.[S5-S8]

Water Contact Angles Measurements

Static water contact angles were measured by using a drop shape analysis system-Kruss DSA 100. Six drops of 3 µl water were automatically placed on the sample. The software allowed for calculating the contact angle between a drop and the sample from an image of the drop taken by a digital camera. The contact angles for the hydrophobic pure CNTs, PEMAc@CNTs95, PEMAc@CNTs90, PEMAc@CNTs80, PAA@CNTs90, PVA@CNTs90, PVAc@CNTs90 and PEG@CNTs90 were 148°, 142°, 140°, 113°, 132°, 86°, 139° and 145°, respectively. These results revealed that these polymers with oxygen-containing groups were coating on the surface of CNTs. Nevertheless, the coating layer thicknesses were too thin to manifest the precise hydrophilicity compared with the pure polymers of PEMAc (85°), PAA (80°), PVA (70°), PVAc (71°) and PEG (70°).[S9]

Electrochemical Testing

All electrochemical measurements were performed on CHI760E electrochemical workstation (Shanghai, China) with a typical three-electrode cell. A glassy-carbon electrode (GCE) with a diameter of 5 mm was used as the working electrode. A platinum foil electrode was used as the counter electrode, whereas an Ag/AgCl electrode was served as the reference electrode. The linear sweep voltammetry (LSV) and the rotating ring-disk electrode (RRDE) with GC disk (0.247 cm^2) and Pt ring (0.186 cm^2) with a 5 mV s^{-1} scan rate were performed at a rotation rate of 1600 rpm in 1 M KOH solution under continuous purging with N_2 before testing at room temperature. For the fabrication of the working electrode, the as-synthesized polymer@CNT catalyst was anchored onto the GCE surface by using nafion glue (5 wt%, Sigma-Aldrich) and dried naturally. To achieve a fair performance comparison, the amounts of Nafion in each test was 2 µl (5 wt% Nafion, Sigma-Aldrich) similar with some previous reports.[S10] All potentials reported in this work were calibrated against the reversible hydrogen electrode (RHE) using equation $E_{RHE} = E_{Ag/AgCl} + 0.210 + 0.059$ pH, where E_{RHE} is the potential calibrated against the RHE and $E_{Ag/AgCl}$ is the potential performed against the Ag/AgCl reference electrode. The linear portions of the Tafel slopes are derived from the polarization curves in the light of the Tafel equation, η = blog$j$ + a, where η is the overpotential, j is the current density, and b is the Tafel slope.[S11] All the electrochemical measurements were collected with 100 % IR drop compensation unless stated otherwise. The mass loading during OER testing is fixed at 0.3 mg cm^{-2}. Our mass loading of 0.3 mg cm^{-2} was very normal, similar with many previous reports (see details in Table S2 and Table S3 in supporting information)

Electrochemically Active Surface Area

The calculation of electrochemically active surface area (ECSA) is based on the measured double layer capacitance of the PEMAc@CNTs90 on glassy carbon RDE in 1 M KOH according to previously published method.[S12, S13] Briefly, a potential range where no apparent Faradaic process happened was determined firstly using the static CV. The charging current i_c was measured from the CVs at different scan rates, as shown in Fig S6. The relation between i_c, the scan rate (v) and the double layer capacitance (C_{DL}) was given in eq 1.

$$i_c = vC_{DL} \qquad (1)$$

Therefore, the slope of i_c as a function of v gives a straight line with the slope equal to C_{DL}. The C_{DL} of pure CNTs and PEMAc@CNTs90 measured by the scan rate dependent CVs are 0.16 and 3.45 mF (see Fig. S6). For the estimation of ECSA, a specific capacitance (C_s) value C_s= 0.040 mF cm^{-2} in 1 M NaOH is adopted from previous reports,[S12-S14] the ECSA values for pure CNTs and CNTs@polymer are calculated to be about 4 and 86 cm^2 according to the equation: ECSA=C_{DL}/C_s, following the well-documented method in the literature.[S12-S14] The obtained ECSA value of pure CNTs in our case is similar to that of previously reported CNT.[S12]

Faraday Efficiency Measurement[S15]

Faraday efficiency was tested using volumetric method. The produced O_2 over the catalyst loaded carbon fiber paper (CFP) (~1.0 cm^{-2}) was accumulated in a 10 ml graduated tube, which was filled with the electrolyte. Current dominated electrolysis was executed at 10 mA cm^{-2} for about 2 h under ambient conditions (20℃, 1 atm). The time was recorded at each 0.3 ml of O_2. The collected charges going through the working electrode, in the meantime, were reckoned via current x time. The collected gas was sampled with a Hamilton syringe and detected by using gas chromatograph (Agilent 7820A) to evaluate its purity. From the GC spectra, O_2 could be the only gaseous product detected, indicating the gas products had no other impurities.

Determination of Turnover Frequencies

Turnover Frequencies (TOF_S) of the OER catalysts were estimated by previously reported methods,[S15, S16] and the following formula was used.

$$TOF = \frac{J \times A}{4 \times F \times N}$$

Where J is the current density at a given overpotential ($\eta = 300\,\mathrm{mV}$), A is the geometric surface area of the electrode, F is the Faraday constant (a value of 96485 $\mathrm{C{\cdot}mol^{-1}}$), and N is the number of moles of active sites on the electrode.

For PEMAc@CNTs90, OER current density at $\eta = 300\,\mathrm{mV}$ from LSV polarization curve in 1 M KOH is about 11.3 $\mathrm{mA{\cdot}cm^{-2}}$. Since the diameter of glassy-carbon electrode (GCE) in our study is 5 mm, the geometric surface area of the electrode (GCE) is calculated to be 0.196 $\mathrm{cm^2}$. In our case, the defects on the side walls of CNTs are considered to be active sites. According to previous reports,[S17, S18] the defects in graphene plane can be quantified by Raman spectroscopy via plotting the I_D/I_G data as a function of the average distance between defects L_D. Hence, the defects amounts on the side walls of CNTs could be estimated from Raman spectroscopy. The I_D/I_G of pure CNTs is 1.02 and L_D is thus determined to be 10 nm while 1 nm is unreasonable.[S17] Considering L_D between defects is determined to be 10 nm, the defects could be abstracted to circles with the diameter of 5 nm packing on the surfaces of CNTs. Therefore, the possession area for each defect is calculated to be about $5\sqrt{3}\,nm \times 10\,nm = 86.6\,nm^2 = 8.66 \times 10^{-17}\,m^2$.

The surface area of CNTs on the electrode is derived from the density of CNTs. Surface area =

$$\frac{mass\ loading\ of\ CNTs\ on\ the\ electrode\ /\ density\ of\ CNTs}{\pi \times (average\ radius\ of\ CNTs)^2} \times \pi \times diameter\ of\ CNTs =$$

$$\frac{0.3\,mg{\cdot}cm^2 \times 0.196\,cm^2\ /\ 60\,g{\cdot}L^{-1}}{\pi \times (5\,nm)^2} \times \pi \times 10\,nm = 3.92 \times 10^{-1}\,m^2$$

The number of moles of defects on the electrode is calculated to be:

$$\mathrm{N}_D = \frac{Surface\ area\ of\ CNTs}{Possession\ area\ of\ single\ defect \times 6.023 \times 10^{23}\,mol^{-1}}$$

$$= \frac{3.92 \times 10^{-1}\,m^2.}{8.66 \times 10^{-17}\,m^2 \times 6.023 \times 10^{23}\,mol^{-1}} = 7.52 \times 10^{-9}\,mol$$

Our theoretical results in Supporting Information (Fig. S16) have confirmed that the SW defect is the most active sites and also the predominant defect for CNTs.[S19] Thus, the SW defect has the dominant contribution for OER. In this context, we assume that all the defects are the SW defects with two active carbon atoms (see Fig. S16), the minimum TOF could be estimated as:

$$TOF_{min} = \frac{J \times A}{4 \times F \times 2N_D} = \frac{11.3\,mA \cdot cm^{-2} \times 0.196\,cm^2}{4 \times 96485\,\mathrm{C \cdot mol^{-1}} \times 2 \times 7.52 \times 10^{-9}\,mol} \approx 0.38\,s^{-1}$$

Following similar method, the TOF_{min} of PEMAc@CNTs80, PEMAc@CNTs95, Pure CNTs, PVAc@CNTs, PVA@CNTs, PAA@CNTs and PEG@CNTs are calculated to be 0.124 s^{-1}, 0.0493 s^{-1}, 0.00709 s^{-1}, 0.0618 s^{-1}, 0.109 s^{-1}, 0.132 s^{-1} and 0.049 s^{-1} respectively.

Density Functional Theory Calculations

The DFT calculations were performed by using Dmol3 package in Materials Studio of Accelrys Inc.

The generalized gradient approximation (GGA)[S20, S21] with the Perdew-Burke-Ernzerhof (PBE) exchange-correlation functional was adopted. An all-electron double numerical basic set was applied with polarization functions (DNP).[S22] Noncovalent interactions correction was used for all calculations. The convergence tolerance for geometry optimization quality was set to fine and the convergence tolerances of energy, force, and displacement were 1×10^{-5} Ha, 2.0×10^{-3} Ha/Å, and 5.0×10^{-3} Å, respectively.

Simulation models

To stimulate the curving surface of CNTs, a considerable size of graphene cluster was carved to form (100,100) armchair carbon nanotube model with a diameter of 15 nm. Such diameter was matched with the outer surface of multi-walled carbon nanotubes we used. Next, the terminal carbon dangling bond was fulfilled with hydrogen atoms, and the position of these hydrogen atoms were optimized with all carbon atoms frozen in their position. Subsequently, a second geometry optimization was processed with freezing the position of the hydrogen atoms and the peripheral carbon atoms they bonded. Throughout the rest of the calculation, the hydrogen atoms and peripheral carbon atoms were constrained to maintain the curvature. Herein, a hydrogen terminated curved graphene cluster was obtained to stimulate the outer surface of multi-walled carbon nanotubes. However, the long macromolecular chains were not feasible for the DFT calculation, they were simplified to be small molecule derived from the repeating units, and was naturally placed above the curved graphene clusters model already built. The central carbon atoms of the Stone-Wales defect were thought to be the most favored adsorption sites for oxygenated intermediates involved in OER because of their positive charge.

The four electron oxidation mechanism[S23] for OER employed here is described as follows:

$$H_2O(l) + * \leftrightarrow *OH + H + e^-$$

$$*OH \leftrightarrow *O + H + e^-$$

$$*O + H_2O(l) \leftrightarrow *OOH + H + e^-$$

$$*OOH \leftrightarrow O_2(g) + H + e^-$$

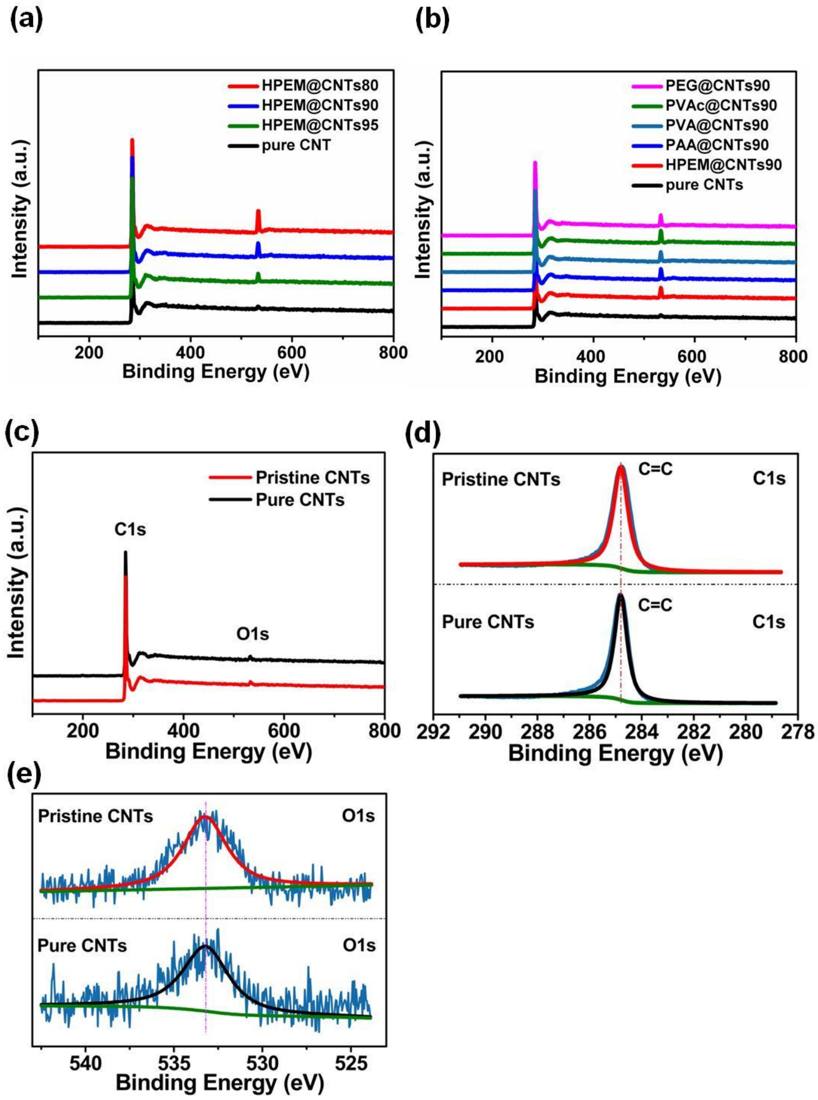

Fig. S1 XPS spectra for pure CNTs, PEMAc@CNTs80, PEMAc@CNTs90, PEMAc@CNTs95 (a), and for PAA@CNTs90, PVA@CNTs90, PVAc@CNTs90, PEG@CNTs90 (b), and the comparison for pristine and pure CNTs (c), high resolution XPS C1s spectra (d) and O1s spectra (e) obtained with pristine and pure CNTs, respectively.

In order to further explore the surface chemistry of the as-produced samples, X-ray photoelectron spectroscopy was performed. As shown in Fig. S1a, a pronounced C1s peak was observed for the purified CNTs, while the presence of a trace amount of O was possibly credited to the incorporation of physically absorbed oxygen.[S24-S27] As clarified in the literatures,[S24, S25] CNTs are well-known to be susceptible to oxygen adsorption even at pressures as low as 10^{-8} to 10^{-10} Torr, typical for the XPS measurements. This will inevitably lead to the presence of a trace amount of oxygen (atomic ratio of O/C: 0.01-0.04 %) physically absorbed onto CNT according to the literature.[S24 S25] In our case, the XPS spectrum of purified CNTs is very similar to that of pristine CNTs (Fig. S1c) and gives a trace amount of oxygen with rather low atomic ratio of O/C (0.014 %), even showing a decrease of the oxygen amount as compared to as-received pristine CNTs (O/C: 0.018 %). This indicates that our purification treatment by HCl is indeed a non-oxidative process, as demonstrated in previous studies.[S4] In fact, the high resolution XPS C1s spectrum for our purified CNTs is almost identical to those of pristine CNT (Fig. S1d) and highly ordered pyrolytic graphite (HOPG)[S24] and can be best fitted into only one C=C peak at 284.7 eV without any other oxygen-carrying components at 286-289 eV, implying that the nanotube structure is indeed free from oxygen groups.[S24] Furthermore, purified CNTs and pristine CNTs have similar high-resolution O1s spectrum and contains only a symmetrical O1s peak at 533.2 eV, which is attributed to the physically absorbed oxygen on the CNT surface due to air exposure according to the literature.[S26] Taken together, all these results indicate that the rather weak oxygen signal in the XPS spectrum of our purified CNTs is credited to the physically absorbed oxygen, which excludes the presence of surface oxygen groups (*i.e.* C-O, C=O) on our CNT graphitic structure.[S24-S26]

Upon PEMAc modification, the intensity of the O1s peak significantly increased and the atom ratio of C/O was reduced from 71 to 10 (Fig. S1b), which arises from the polymer chain with oxygen-containing groups anchored on the nanotube surface. Similar results were observed for other polymer@CNT composite samples, as shown in Fig. S1b. Notably, no peaks from possible metal impurities and heteroatom dopants (such as N at 398-402 eV, Cl at 200 eV) was detected in the XPS spectra for pure CNTs and the polymer@CNT composites, indicating that our purified CNT samples do not incorporate any dopants, similar with previously-reported HCl-treated CNTs without possible N and Cl impurities,[S4] and the metal residues in pristine CNTs, if any, have been largely removed by the purification treatment.

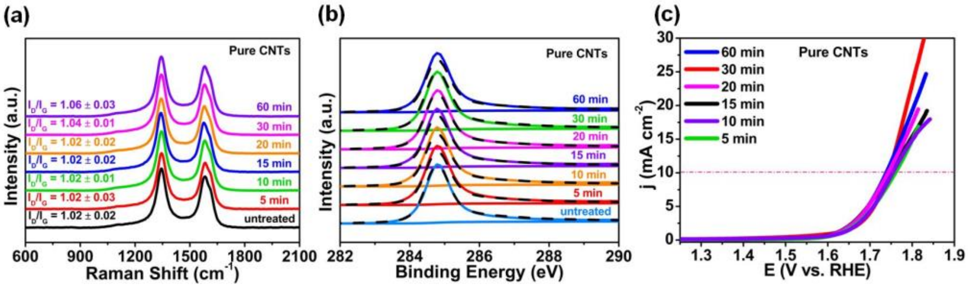

Fig. S2 (a) Raman and (b) XPS spectra of the CNT powder without sonication treatment, pure CNT membranes produced with different sonication time and (e) the corresponding LSV curves in 1 M KOH solution, respectively. For each sample, we took 5 different positions for Raman characterization, the I_D/I_G took the average value obtained for 5 different positions.

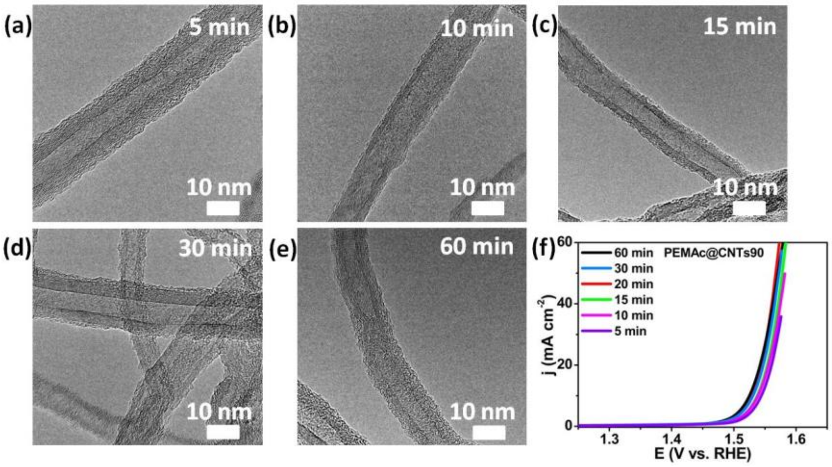

Fig. S3 Representative HRTEM images of PEMAc@CNTs90 produced with different sonication time: (a) 5 min, (b) 10 min, (c) 15 min, (d) 30 min, (e) 60 min and (f) the LSV curves for the samples produced with various sonication times of 5, 10, 15, 20, 30, 60 mins in 1 M KOH solution, respectively.

We have performed the detailed study regarding the sonication effect and our experimental results have excluded the effect of sonication on the structure and OER activity of the nanotubes under our mild sonication condition with a short sonication time, as is the case of our present work. Actually, sonication indeed could affect the surface structure of CNTs. However, the degree of the sonication effect is strongly dependent on energy transfer efficiency of the solvent (the use of water, acetone or ethanol causes much less effect), temperature, sonication power, and sonication time.[S28, S29] In order to prevent the polymer degradation in our study, we used a high frequency, low power sonic bath (Elmasonic, 40 kHz) for sonication of the samples in an ice bath to prepare pure CNT membrane and PEMAc@CNT membrane. Besides, the sonication time was limited to only 20 min and acetone - a high vapor pressure solvent, which can cushion cavitation bubble collapse,[S30] was used as the dispersion solvent to further reduce possible sonication effect, if any. Thus, the sonication process in our study was rather mild, which didn't cause obvious CNT structure damage in consistent with our experimental observation (see Fig. S2a-c and Fig. S3a-f).

More specifically, we first produced a series of pure CNT membrane with various sonication times from 5, 10, 15, 20, 30, to 60 mins using a high frequency, low power sonic bath (Elmasonics, 40 kHz). Thereafter, we characterized the structure and composition of the sonicated CNT samples by Raman and XPS spectroscopy and compared with that of the CNT powder without any sonication treatment. It is known that Raman spectroscopy is a powerful instrument for quantification of defects in carbon materials via plotting the intensity ratio of the characteristic D band vs. G band (I_D/I_G) as a function of the average distance between defects L_D.[S17, S18] According to Ref. S17, a larger value of I_D/I_G reveals a smaller L_D for a higher density of defects. For each sample, we took 5 different positions for Raman characterization, the I_D/I_G took the average value obtained for 5 different positions. As can be seen from our Raman results (Fig. S2a) with respect to those of the CNT powder without sonication, the I_D/I_G values for the CNT powder without any sonication treatment and the pure CNT membranes produced with the sonication time less than 30 min are almost identical. This indicates that our mild sonication condition with a short sonication time of 20 min should not introduce any structural defect on the nanotube surface. Furthermore, the corresponding XPS results (Fig. S2b) show that all the pure CNT membranes produced with sonication have almost the same high resolution XPS C1s spectrum as that of the CNT powder without sonication, which can be only fitted with one C-C/C=C peak without any oxygen component over 286-290 eV, indicating, once again, that our mild sonication condition did not generate any surface oxygen group on the nanotubes. Thus, the sonication effect on the nanotube surface structure in our study can be excluded. On the other hand, as seen from electrochemical results (Fig. S2c), the onset potential and the overpotential at 10 mA cm^{-2} of the pure CNT membrane after sonication for less than 30 min did not change with the sonication time. This further confirms that there is no sonication effect under our mild sonication conditions with a short sonication time.

Under the above-mentioned mild conditions, we have also produced a series of PEMAc@CNT membranes with different sonication time of 5, 10, 15, 20, 30, and 60 min, respectively. Due to the presence of the polymer adsorbed onto the nanotube surface, it was difficult to investigate the structural change of the nanotube by Raman and XPS spectroscopy. In this particular case, therefore, we performed the HRTEM and electrochemical characterization. Our HRTEM observation did not reveal any shortening or unzipping of the PEMAc@CNTs even after sonication for 60 min (Fig. S3). Likewise, the corresponding electrochemical results (Fig. S3) show no sonication-time-dependence for both the onset potential and the overpotential at 10 mA cm^{-2}, when the sonication time is less than 30 min. Once again, these results further confirm that the effect of the sonication in our case is negligible under our mild sonication conditions with a short sonication time. In fact, the nanotubes were dispersed in the polymer solution by sonication during the preparation of PEMAc@CNT. The dispersed nanotubes were then wrapped with a layer of polymer (see HRTEM in Fig. 1), which further reduced the sonication effect on the nanotube structure.

Overall, the above experimental results and discussions clearly indicate that the sonication effect is negligible under mild sonication conditions with a short sonication time, as is the case of our present study.

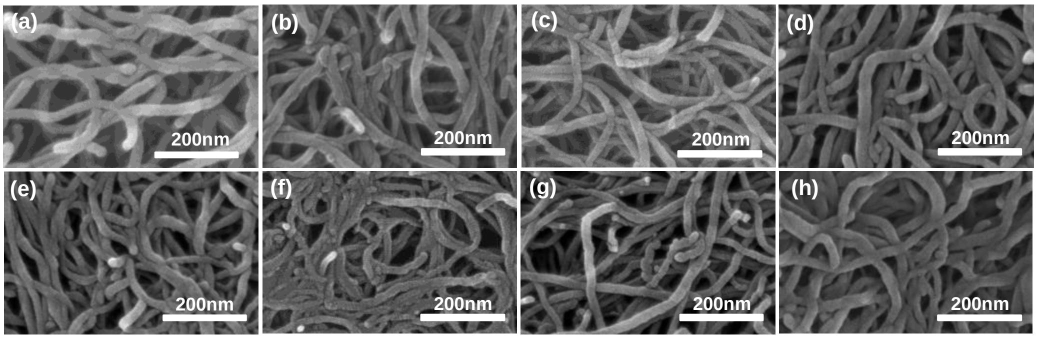

Fig. S4 SEM images of samples: Pure CNTs (a), PEMAc@CNTs80 (b), PEMAc@CNTs90 (c), PEMAc@CNTs95 (d), PAA@CNTs90 (e), PVA@CNTs90 (f), PVAc@CNTs90 (g) and PEG@CNTs90 (h).

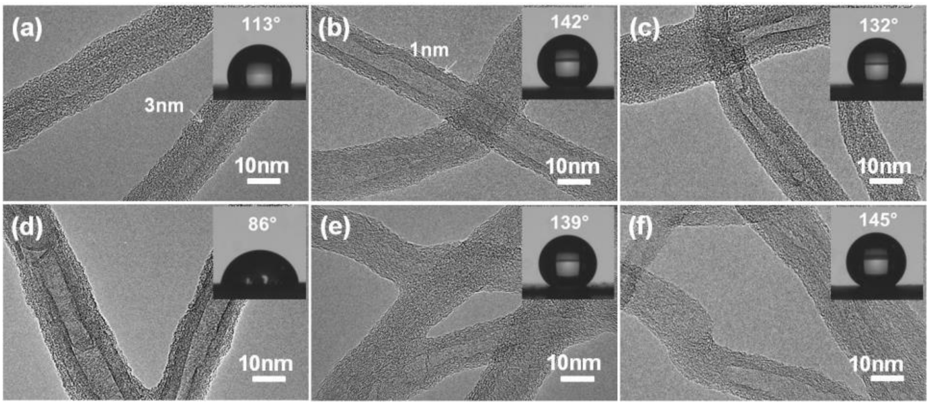

Fig. S5 HRTEM images of samples (the water contact angles are shown in the inset of upper corners): PEMAc@CNTs80 (a), PEMAc@CNTs95 (b), PAA@CNTs90 (c), PVA@CNTs90 (d), PVAc@CNTs90 (e) and PEG@CNTs90 (f).

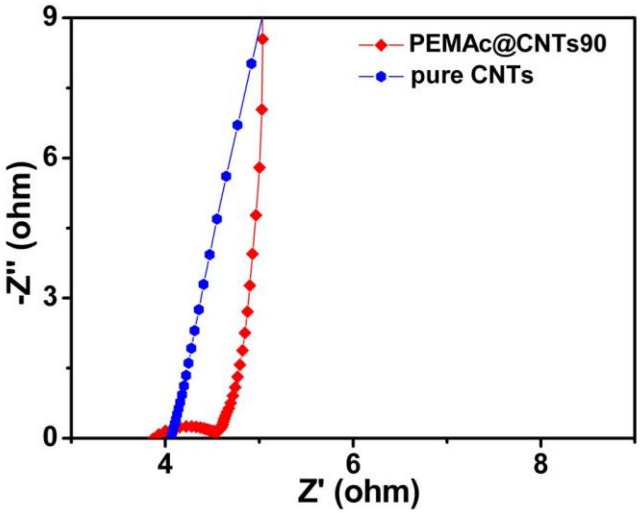

Fig. S6 Nyquist plots of OER on pure CNTs and PEMAc@CNTs90, respectively. The Nyquist plots of both materials exhibited a similar series resistance, indicating that the ultrathin polymer coating layer has little effect on the conductivity of the composite system.

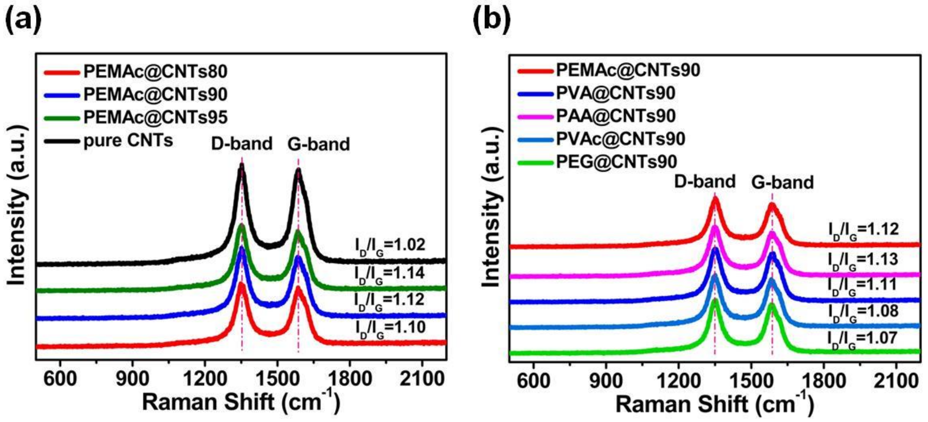

Fig. S7 Raman spectra obtained with PEMAc@CNTs of different ratios (a), and with various polymers (b).

Raman spectra for pure CNTs and PEMAc@CNTs shown in Fig. S7a revealed almost the same pattern with the D and G bands centered at ~1350 cm^{-1} and ~1580 cm^{-1} respectively. Notably, the peak positions for both D and G bands almost remained unchanged after polymer wrapping, implying that the noncovalent modification of polymers does not affect the graphite structure of CNTs and the intrinsic electronic structure associated with CNTs is not destroyed/altered.[S27, S31, S32] No shift in peak positions verifies that there is indeed no charge-transfer interaction between two components,[S27, S31, S32] since the presence of charge-transfer interaction between the CNT and the polymer can be manifested by the shift of the G band position, as demonstrated in previous reports.[S27, S31] Relative to pure CNT, the slight increase of the intensity ratio of the D/G band (I_D/I_G) for the composite system indicated the effective polymer coating on the nanotubes.[S32] Similar results were observed for other composite samples, as shown in Fig. S7b.

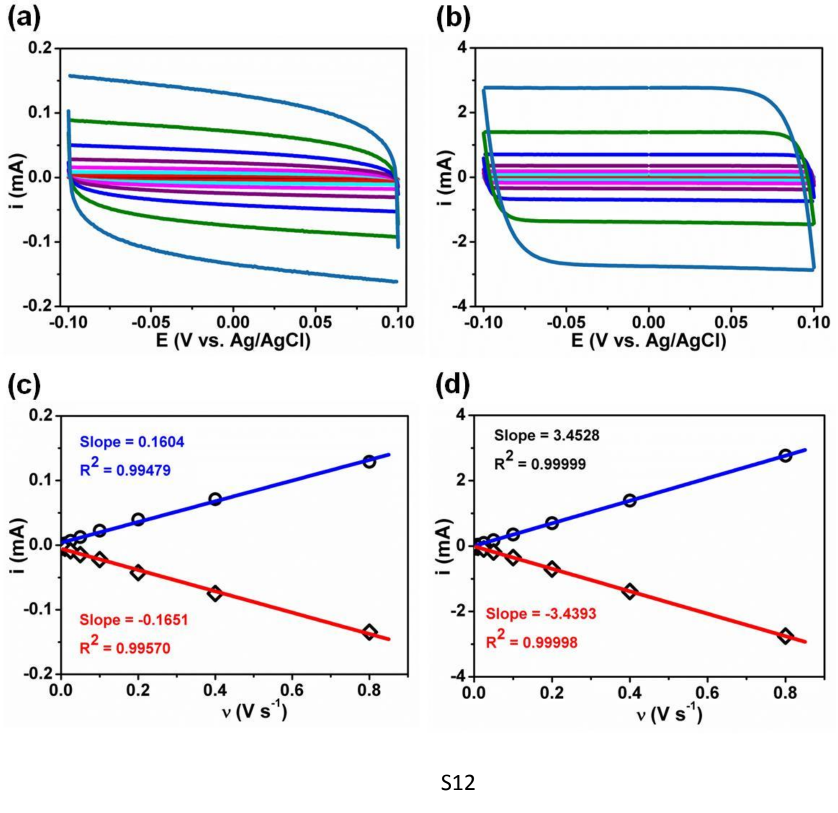

Fig. S8 (a-b) Cyclic voltammograms obtained with (a) the pure-CNTs and (b) PEMAc@CNTs90 loaded glassy carbon electrodes in the capacitance current range (-0.1 V ~ 0.1 V vs. Ag/AgCl) at scan rates of 5, 10, 25, 50, 100, 200, 400 and 800 mV, respectively. (c-d) The cathodic (square) and anodic (circle) capacitance currents measured at 0 V vs. Ag/AgCl plotted as a function of scan rate. The double-layer capacitance determined from this system is taken from the average of the absolute value of anodic and cathodic slopes of the linear fits.

The C_{DL} of pure CNTs and PEMAc@CNTs90 measured by the scan rate dependent CVs are 0.16 and 3.45 mF. For the estimation of ECSA, a specific capacitance (C_s) value C_s= 0.040 mF cm^{-2} in 1 M NaOH is adopted from previous reports,[S12-S14] the ECSA values for pure CNTs and CNTs@polymer are calculated to be about 4 and 86 cm^2 according to the equation: ECSA=C_{DL}/C_s, following the well-documented method in the literature.[S12-S14] The obtained ECSA value of pure CNTs in our case is similar to that of previously reported CNT.[S12] Similar to many previous reports,[S12, S33] the ECSA of our samples is estimated based on the measured electric double-layer capacitance (C_{DL}) in 1 M KOH. As demonstrated in previous reports, the C_{DL} is often linearly proportional to the effective surface area (ECSA). That is to say, the improvement in ECSA for our CNT wrapped with PEMAc can be explained by the increase of C_{DL}. Actually, electric double-layer capacitance is based on the charge separation occurring at an electrode-electrolyte interface when voltage is applied, where electric charges are accumulated on the electrode surfaces and ions of opposite charge are arranged in the electrolyte side. In our case, the increased double-layer capacitance C_{DL} for our PEMAc wrapped CNT mainly originates from in the following aspects: (1) Our PEMAc serves an anionic polyelectrolyte in KOH and is negatively charged. As proposed by previous studies,[S34, S35] the polyelectrolyte coating layer on carbon structures can accommodate adsorption of more ions at the interface by specific adsorption process and facilitate an excess specific double layer capacitance C_{DL} due to the local changes of electronic charge density. (2) As demonstrated in previous studies,[S36, S37] improved electrolyte wetting behavior commonly improves the charge-discharge rate and allows one to achieve higher specific capacitance value. However, the pure CNT has not only a hydrophobic nature but also a weak affinity with KOH electrolytes. By contrast, PEMAc coating improves the surface wettability of the CNT electrode due to the hydrophilic nature of PEMAc, as evidenced by the reduced surface contact angel (See Figure 1). As proposed by the literature,[S36] such improved wettability behavior for PEMAc@CNT will enhance C_{DL} of the carbon through improved pore access and greater surface utilization.

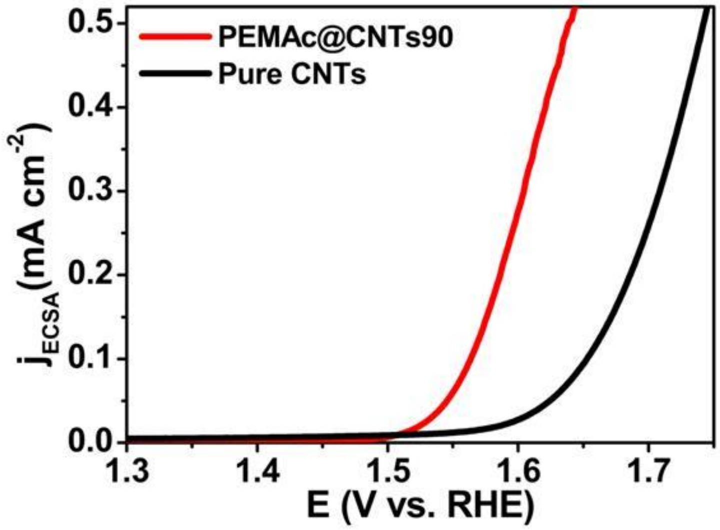

Fig. S9 The polarization curves of PEMAc@CNTs90 and pure CNTs corrected for electrochemically active surface areas (ECSA) calculated by LSV curves.

As can be seen from Fig. S9, although the electroactive surface area (ECSA) of pure CNTs increases from 4 to 86 cm^2 after polymer wrapping, the corrected LSV data normalized for the ECSA shows that the polymer/CNTs catalyst is still much superior to that of pure CNTs. For example, at 0.5 mA/cm^2 $_{ECSA}$, there is still a 105 mV overpotential decrease for polymer@CNT (Fig. S9). At the overpotential η = 350 mV, the polymer@CNT catalyst delivers an OER j_{ECSA} of 0.169 mA cm^{-2}, much higher than that of pure CNT (0.018 mA cm^{-2}) and many previously reported OER catalysts such as surface oxidized CNTs,[S12] electrodeposited CoOx and CoPi composites.[S38] This indicates that the increase in ECSA is not the sole cause for improved OER activity in our composite catalyst and the wrapping polymer indeed intrinsically facilitates the OER at CNTs.

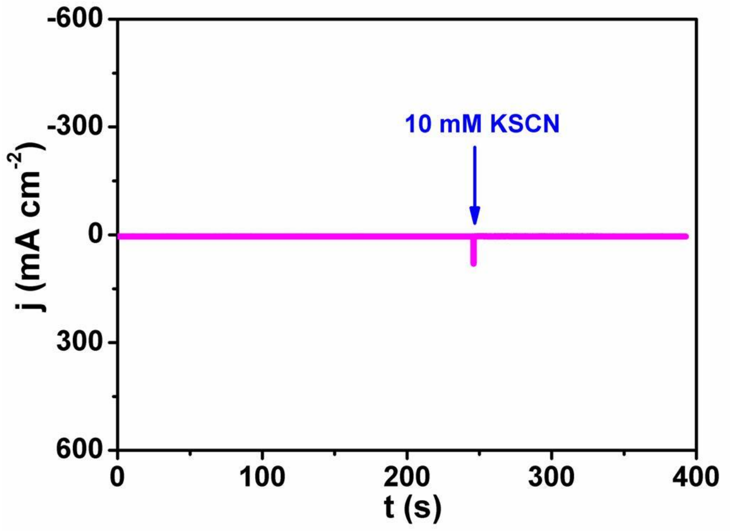

Fig. S10 Chronoamperometric response of PEMAc@CNTs90 in 1 M KOH solution with the addition of 10 mmol KSCN.

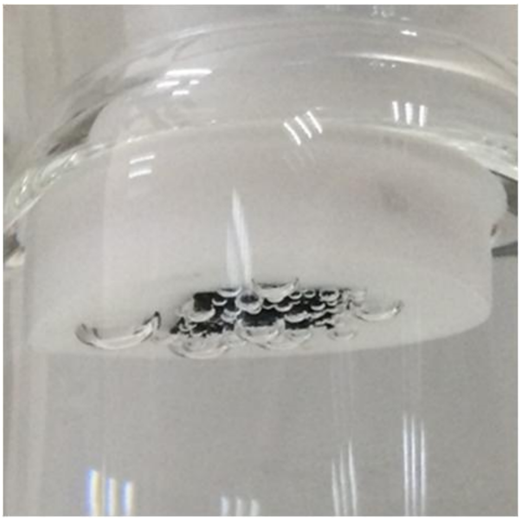

Fig. S11 Photograph of PEMAc@CNTs90 loaded rotating disk electrode after LSV scan in the OER region, showing O_2-bubbles on the electrode surface.

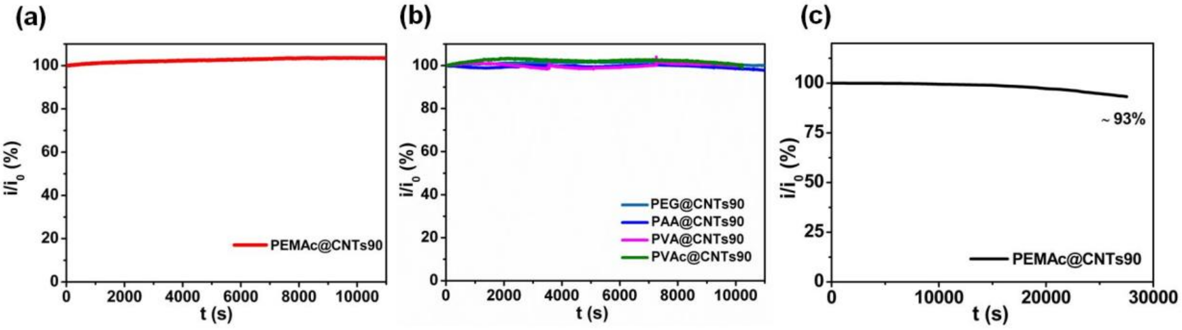

Fig. S12 Chronopotentiometric curves obtained at constant current (*j* = 5 mA cm^{-2})

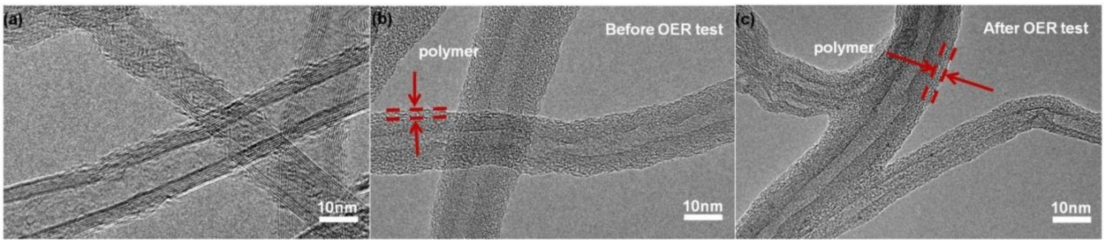

Fig. S13 HRTEM image of pure CNTs (a), PEMAc@CNTs90 before (b) and after (c) long-term OER test, respectively.

After long-term i-t testing (>10000 s), the PEMAc@CNTs90 catalyst is investigated by the HRTEM observation. The HRTEM imaging (Fig. S13c) clearly revealed the presence of the polymer coating layer on the CNT surface, which verifies the excellent stability of the composite catalysts in 1.0 M KOH.

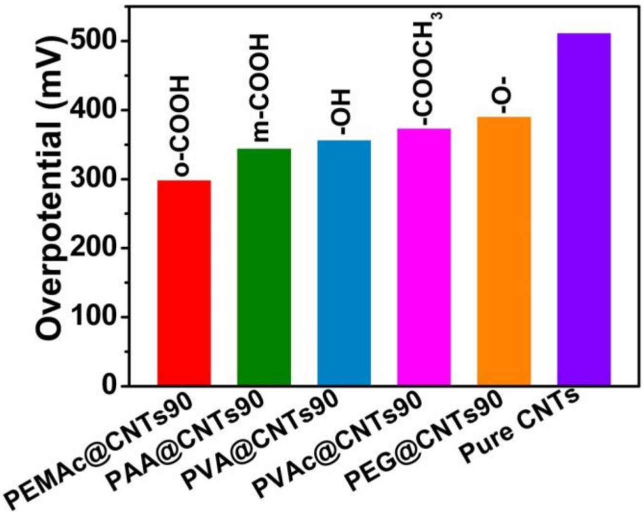

Fig. S14 OER overpotentials of various polymer@CNTs electrocatalysts at 10 mA cm^{-2} in 1 M KOH.

The polymer-wrapping-induced boosting of the OER performance at pure CNTs was observed from a certain class of various polymers with polar oxygen groups, including PEMAc, PAA, PVAc, PVA, and PEG. These polymer@CNTs electrocatalysts afforded various OER overpotentials at 10 mA cm^{-2}, which should be ascribed to the difference of the interaction between various polar oxygen groups (-COOH, -OH, -OOCH$_3$,-O-) from the polymer and H-carrying OER intermediates (OH*, OOH*).

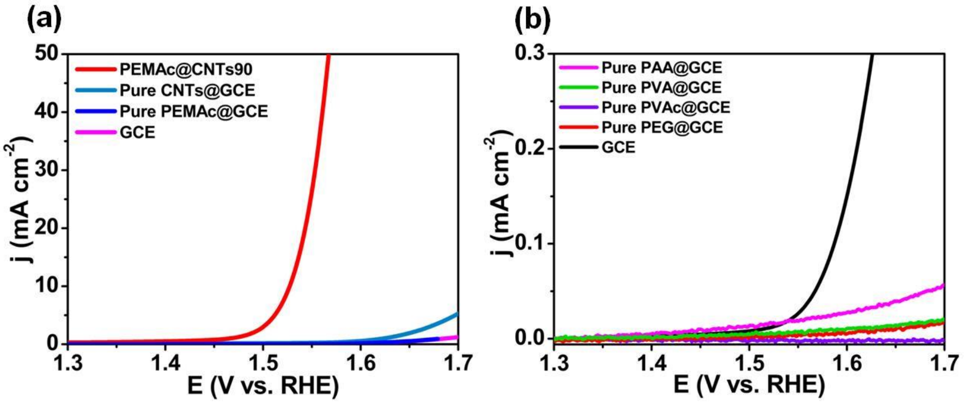

Fig. S15 (a) LSV curves of PEMAc@CNTs90, pure CNTs, pure PEMAc on glassy carbon electrodes (GCE) and bare GCE in 1 M KOH solution; (b) LSV curves of pure PAA, PVA, PVAc, PEG on GCE and bare GCE in 1 M KOH.

As can be seen from Fig. S15, all pure polymer@GCE electrodes showed negligible current density, even much lower than that of bare GCE electrodes, which verifies that all these polymers alone are indeed electrochemically inert without OER activities.

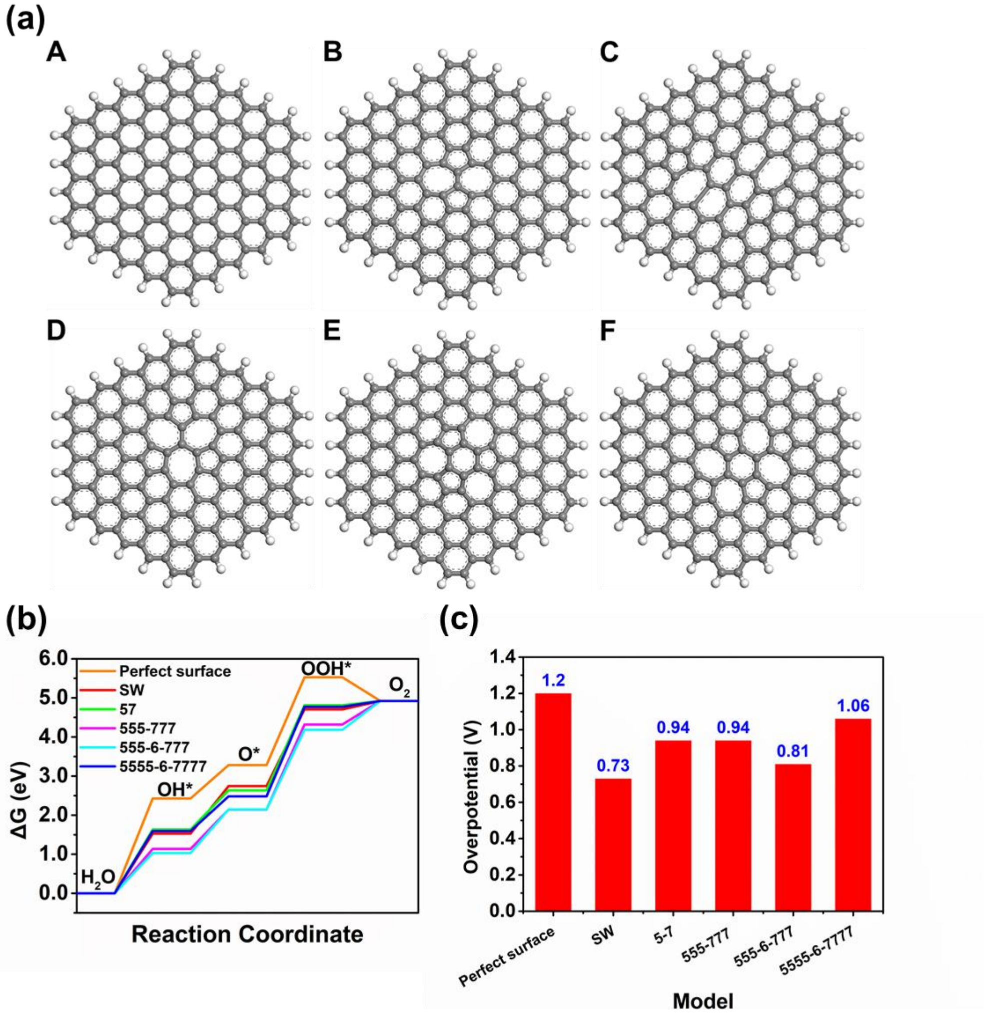

Fig. S16 (a) Models for DFT calculations. We have performed DFT stimulation on (A) perfect graphitic surface and several types of defects on the sidewall of carbon nanotubes, including (B) Stone-Wales (SW) defect (55-77), (C) 5-7, (D) 555-777, (E) 555-6-777 and (F) 5555-6-7777. Here the 5, 6, and 7 refer to the pentagon, hexagon, and heptagon carbon ring in the defect configuration. (b) Free energy diagrams of OER at U = 0 V for CNTs with perfect graphitic surface and different types of defects as active sites respectively. (c) The calculated OER overpotentials for perfect graphitic surface and different defect sites. Among them, the topological SW configuration shows the smallest overpotential towards OER. Also, according to the literature,[S39] the SW is considered to be the most common and predominant defect on CNTs, thus SW defects in our case are recognized to be the OER active sites in our following calculating models.

For our composite catalysts, the employed polymers alone are electrochemically inert without OER activity (see details in Fig. S15), and have no charge-transfer capability as verified by Raman spectra (see details in Fig. S7), while even dopant-free CNTs alone can deliver OER activity as demonstrated by many previous reports.[S40, S41] Hence, the OER active sites for our composite should come from the CNTs. Previous studies have shown that possible OER active sites for metal-free carbon catalysts can be created by heteroatom-dopants, surface oxygen groups and defective sites induced by chemical functionalization.[S40, S41] Unlike all previous carbon-based OER catalysts, however, our polymer@CNTs catalysts do not destroy/alter the CNTs structure, which excludes the presence of heteroatom dopants and surface oxygen groups on the CNT graphitic structure as evidenced by detailed XPS analysis (see details in Fig. S1). Meanwhile, the role of metal impurities was also ruled out by control experiments, as detailed in Fig. S10 and Table S1. Thus, for our CNTs free from dopants and oxygen groups, there are two possible sites: non-defective sites (perfect surface) and intrinsic topological defects (TDs, *i.e.* pentagon and heptagon carbon rings), while recent studies have identified inherent TDs as effective active sites for OER over dopant (*i.e.* O, N)-free carbon (non-defective perfect sites are ineffective).[S40, S41] Based on the above facts, intrinsic TDs in CNTs are thus considered as the OER active center for our polymer@CNTs catalysts, as also validated by our theoretical calculation (Fig. 5 and S16-18) and supported by recent literature.[S40, S41]

As clearly demonstrated in the literature,[S39] as for CNTs, the conventional types of defects, like vacancies and interstitials, are unlikely to be found in pristine CNTs, while the topological Stone-Wale (SW) defect (5-7-7-5 configuration) is a relatively common type of topological defect in CNT systems and is presumed to be predominant even if CNT synthesis, particularly chemical vapor deposition synthesis, proceeds at lower temperature than typical graphitization.[S39] Despite the fact that the SW defect is the most common and predominant topological defect, we cannot rule out the presence of various topology-changing combinations of 5-7 pairs. Therefore, we have performed DFT stimulation (Fig. S16) on (A) perfect graphitic surface and several types of topological defects on carbon nanotubes, including (B) Stone-Wales defect, (C) 5-7, (D) 555-777, (E) 555-6-777 and (F) 5555-6-7777 pointed out by Ref. S39. As can be seen from Fig. S16b-c, the non-defect sites (perfect surface) are ineffective for OER and give the largest overpotential of 1.2 V, while the topological SW configuration shows the smallest overpotential towards OER among various types of TDs. These results confirm that the SW configuration is the most effective active sites. Considering the SW defect is the predominant TD in CNTs,[S39] in our present case, it is reasonable to conclude that topological SW defects are recognized to be the main OER active sites for our CNT catalyst.

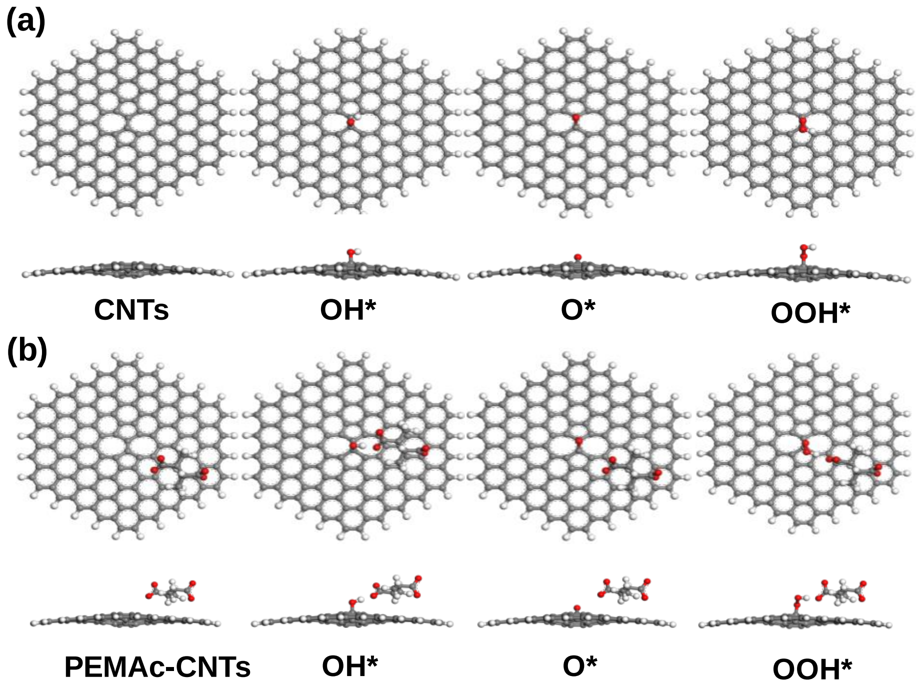

Fig. S17 Models (top and side view) for DFT calculations. (a) Optimized structures of curved graphene clusters model and oxygenated intermediates adsorbates involved in OER. (b) Optimized structures of curved graphene clusters with naturally placed simplified PEMAc molecular and oxygenated intermediates adsorbates involved in OER.

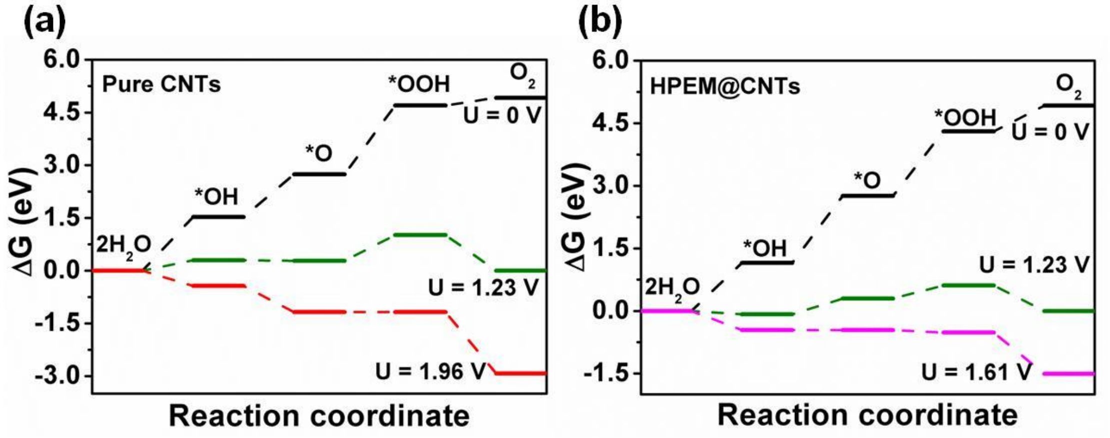

Fig. S18 Standard free energy diagram for elementary reactions of OER over (a) pure CNTs, (b) PEMAc@CNTs with topological SW defects as active centers at pH = 0. For both CNTs and PEMAc@CNTs, the OER are still uphill when the electrode potential is 1.23 V, but when the potential increases to 1.61 V (0.38 V in overpotential) and 1.96 V (0.73 V in overpotential), all elementary reaction steps become downhill over PEMAc@CNTs and pure CNTs respectively, and OER occurs spontaneously over such potential.

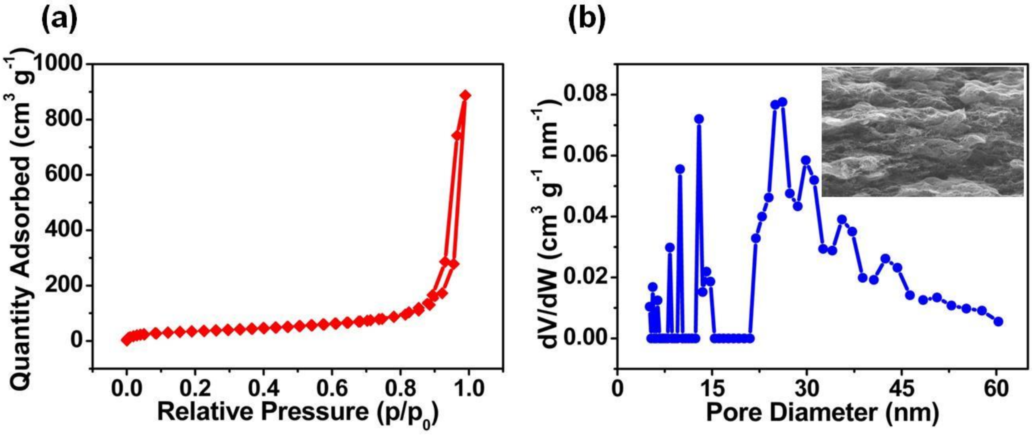

Fig. S19 (a) N_2 sorption isotherms of the PEMAc@CNTs90 composite and (b) pore size distribution, the inset is the cross-sectional SEM image.

The PEMAc@CNTs90 sample shows a Brunauer-Emmet-Teller (BET) surface area of 130 m^2 g^{-1} and a total pore volume of 1.37 cm^3 g^{-1}, contributed by a substantial quantity of mesopores.

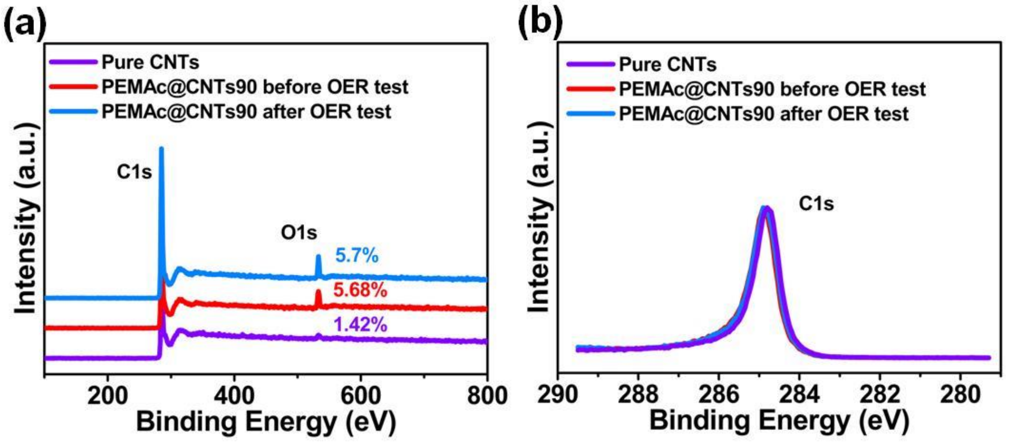

Fig. S20. (a) XPS spectra of pure CNTs, PEMAc@CNTs90 before and after long-term OER test respectively, (b) and the corresponding high resolution XPS C1s spectra.

More recent work has experimentally confirmed that individual MWCNTs will not be electrochemically etched within a certain potential range of ~1.0 - 1.8 V *vs.* RHE in 1 M KOH[S12] and even after long-term OER durability test at 1.72 V, the MWCNTs remained almost unaffected in chemical compositions and structures.[S12] Similar with previous reports regarding carbon-based OER catalysts, [S12, S40, S41] the applied potential range in our case is ~1.0-1.75 V *vs.* RHE, which avoiding possible electrochemical etching of our CNTs at overhigh potential in KOH during the OER test.[S12] This is also confirmed by our experimental observation using TEM (Fig. S13) and XPS (Fig. S20). As can be seen from Fig. S20, no significant change in oxygen content for our composite catalyst was detected after long term OER test. Furthermore, high-resolution C1s spectrum remained almost unchanged after long term OER testing. HRTEM observation in Fig. S13 did not show any detectable damage to the nanotube structure. All these facts verify that our CNT catalyst is rather stable during our OER test with the potential range of ~1.0 - 1.75 V *vs.* RHE, excluding the electrochemical oxidation of the nanotubes in our case.

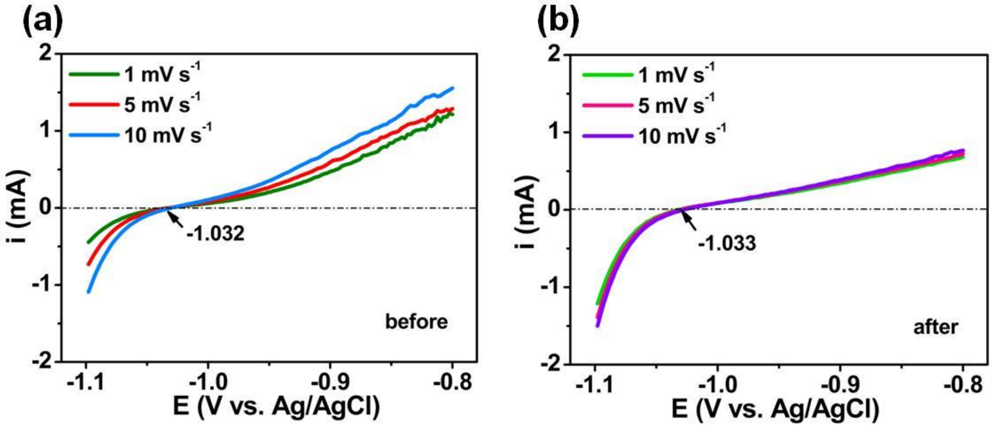

Fig. S21. Linear sweep voltammograms obtained with different scan rates in hydrogen (H_2)-saturated 1 M KOH solution before use (a) and after long-term test (b).

Actually, before and after long-term tests (27000 s), the Ag/AgCl electrode was calibrated in 1 M KOH saturated with hydrogen using Pt plate as the working electrode according to previous reports.[S14b, S42, S43] As demonstrated in the above mentioned references, the potential for RHE scale is the intersection point between the anodic, hydrogen oxidation current and the cathodic, hydrogen evolution current, or the potential crossing the point where the current is zero. In the present work, three zero-crossing points were obtained from three LSV curves at three different scan rates (namely, 1, 5, and 10 mV s^{-1}), and the average potential of these three points was taken as the criterion for the RHE. According to the calibration data in this work (Fig. S21):

Before use: $E_{RHE} = 1.032 + E_{Ag/AgCl} = E_{Ag/AgCl} + 0.206 + 0.059$ pH (pH = 14).

After long-term test: $E_{RHE} = 1.033 + E_{Ag/AgCl} = E_{Ag/AgCl} + 0.207 + 0.059$ pH (pH = 14).

Clearly, the potential of Ag/AgCl after long term testing (27000 s) in our case showed negligible change.

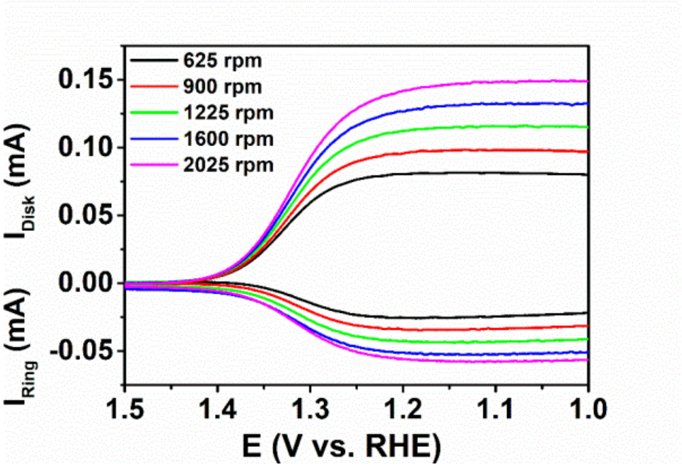

Fig. S22. Rotating ring-disk voltammograms in N_2 saturated 1 mM $K_3Fe(CN)_6$ + 1 M KOH electrolyte at different rotation rates.

The collection efficiency of the rotating ring disk electrode (RRDE) was also determined to be 0.34 by previously reported method.[S44, S45] Rotating ring-disk voltammogram was collected in N_2

saturated 1mM $K_3Fe(CN)_6$ + 1 M KOH electrolyte at a scan rate of 0.05 V s^{-1} at different rotation speed. The Pt ring electrode was potentiostated at 0.7 V vs. Ag/AgCl which is sufficient to rapidly oxidize the product at the ring electrode. Here ferricyanide ($Fe(CN)_6^{3-}$) was reduced to ferrocyanide (($Fe(CN)_6^{4-}$) at disk electrode and oxidized to ferricyanide again at positive potential (0.7 V vs. Ag/AgCl) where the detection of ferrocyanide is diffusion limited. Hence, the collection efficiency could be calculated from the limiting current ratio of ring and disk and could be written as:

$$N = \frac{i_{Limiting,Ring}}{i_{Limiting,Disk}}$$

The value of collection efficiency was measured to be 0.34 independent of rotation speeds.

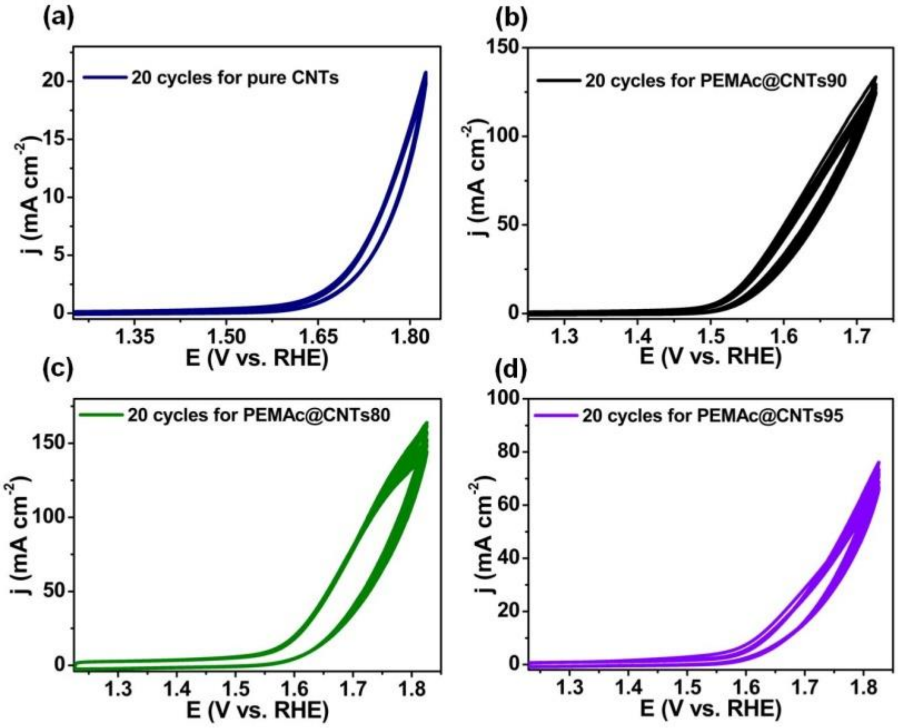

Fig. S23. CV curves with 20 cycles of pure CNTs (a), PEMAc@CNTs90 (b), PEMAc@CNTs80 (c) and PEMAc@CNTs95 (d) at a rotation speed of 1600 rpm at a scan rate of 50 mV/s in 1 M KOH without IR-correction

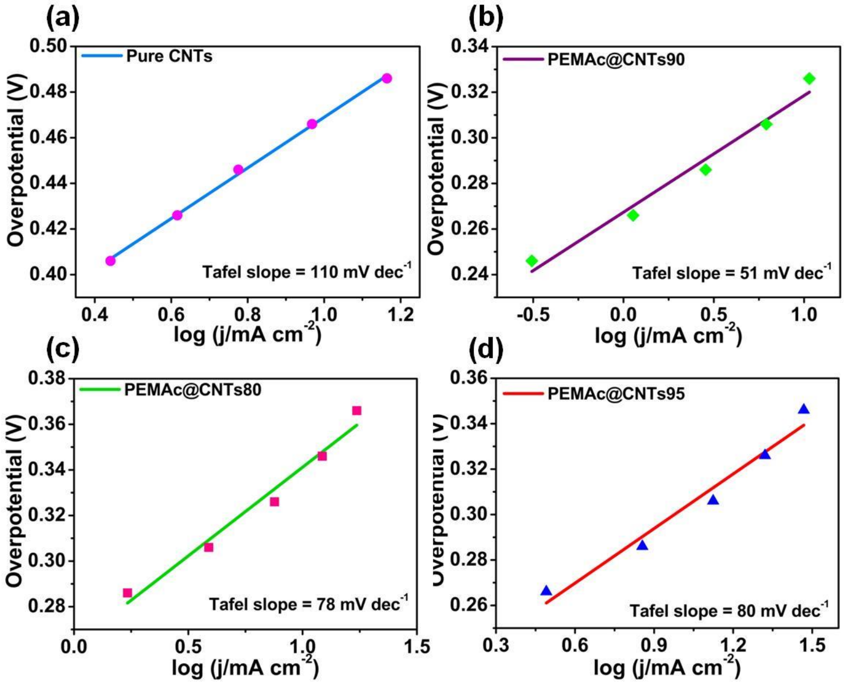

Fig. S24. Steady-state Tafel plots for pure CNTs (a), PEMAc@CNTs90 (b), PEMAc@CNTs80 (c) and PEMAc@CNTs95 (d) during OER.

We have performed steady state polarization method to determine the Tafel slopes. In brief, the steady-state current density for oxygen evolution was collected by controlled potential electrolysis of various catalysts casted on rotating disk electrode (RDE) rotating at 1600 rpm in 1 M KOH. Tafel data were collected by adjusting the electrode potential in fixed decrements of 20 mV with IR drop compensation. The steady-state OER current density was plotted as a function of the applied overpotential for determining the Tafel slope. The Tafel slope measured for PEMAc@CNTs90, PEMAc@CNTs80, PEMAc@CNTs95 and pure CNTs were 51 mV dec^{-1}, 78 mV dec^{-1}, 80 mV dec^{-1} and 110 mV dec^{-1}, respectively.

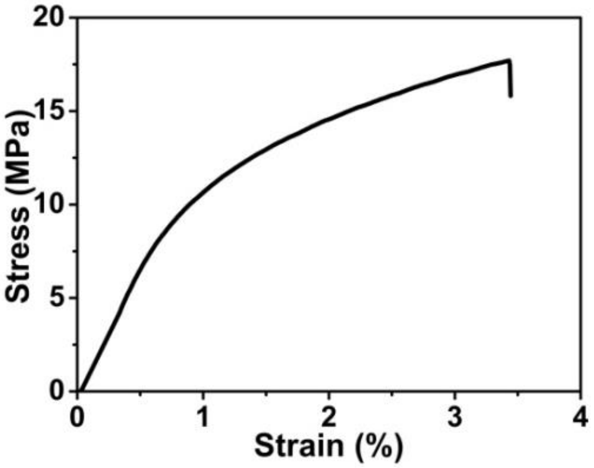

Fig. S25. The stress-strain curve of the PEMAc@CNTs90 membrane. As can be seen from Fig. S25, the membrane exhibits excellent mechanical property with a high tensile strength of 17.6 MPa at a strain of 3.4%, superior to some literature-reported polymer@CNT composite membrane.[S46]

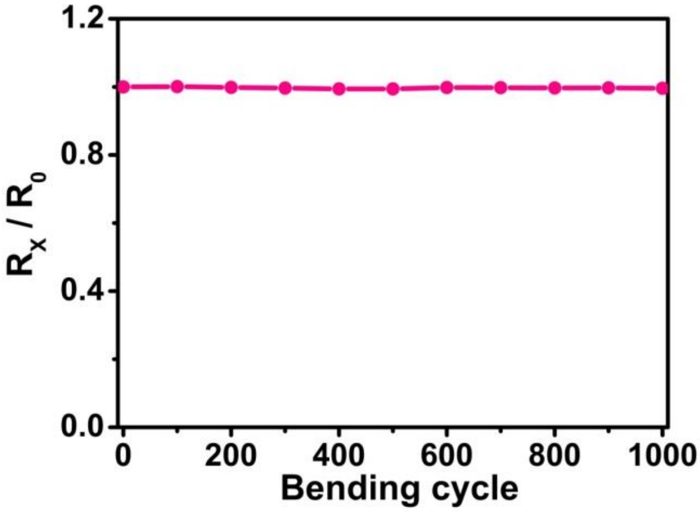

Fig. S26. The resistance variation of the PEMAc@CNTs90 membrane with different bending cycles. R_0 and R_x correspond to the resistances before and after bending, respectively. As can be seen from Fig. S26, no obvious change in the electrical resistance of the membrane was observed after 1000 bending cycles, indicating the excellent mechanical stability of the PEMAc@CNTs90 membrane electrode.

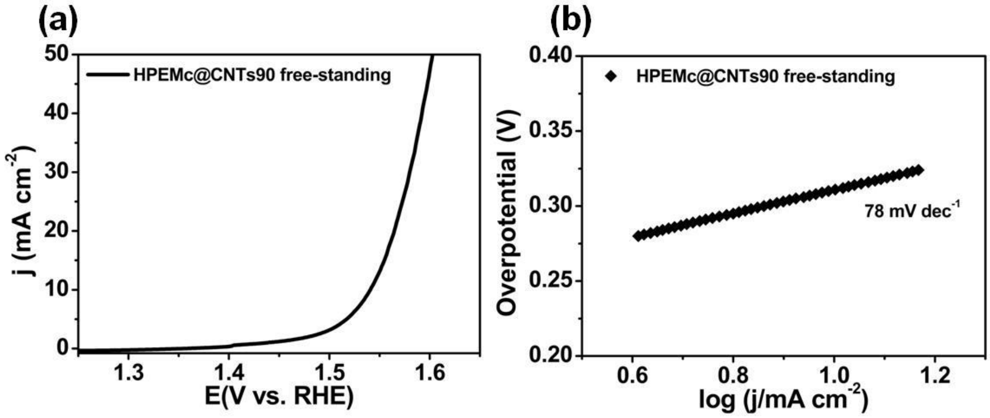

Fig. S27. (a) LSV curves of PEMAc@CNTs90 free-standing membrane directly used as the electrode in 1 M KOH solution and (b) The corresponding Tafel plot. We have also performed the OER test using the optimal PEMAc@CNTs90 membrane directly as the electrode. As can be seen from Fig. S27, the free-standing membrane electrode exhibited good OER performance with a low overpotential of 310 mV at 10 mA cm^{-2}, comparable to the commercial RuO_2 catalysts (294 mV at 10 mA cm^{-2}) on the GCE with similar mass loading.

Table S1. Inductively coupled plasma mass spectrometry (ICP-MS) determination of metal impurities in MWCNTs.

MWCNTs	**Ni/ppm**	**Fe/ppm**
Pristine CNTs	**3.55**	**3310**
Pure CNTs	**1.14**	**960**

Despite the presence of ppm-level of Ni and Fe detected by ICP-MS, our purified CNTs have rather poor OER activity (511 mV at 10 mA/cm^2) in sharp contrast to our polymer@pure CNT composite (298 mV at 10 mA/cm^2), indicating that such trace amount of Fe and Ni residuals in CNT have very little contribution to the OER activity, which is also strongly supported by previous reports.[S12] In Ref. S12, it has been confirmed that residual metals in CNTs, either Ni or Fe, make negligible contributions to the OER activity by a series of control experiments (see Fig. 1A and 3A in Ref. S12). Actually, we further excluded the role of the metal impurities by testing the activity after adding KSCN into electrolytes to poison metal-based active sites (see Fig. S10). As clearly demonstrated in Fig. S10, no activity loss for our composite catalyst was observed after the addition of KSCN, indicating metal-free catalytic active sites.

Table S2. Comparison of selected state-of-the-art metal-free OER electrocatalysts in alkaline solution

Catalyst	Overpotential at 10mA cm^{-2} (mV vs. RHE)	Tafel slope (mV dec^{-1})	Mass loading (mg cm^{-2})	Substrate	Electrolyte	Reference
PEMAc@CNTs90	298	52	0.3	GCE	1 M KOH	This work
RuO_2	294	56			1 M KOH	
PAA@CNTs90	344	99			1 M KOH	
PVA@CNTs90	356	101			1 M KOH	
PVAc@CNTs90	373	81			1 M KOH	
PEG@CNTs90	390	90			1 M KOH	
Pristine CNT	466	95			1 M KOH	
Pure CNT	511	104			1 M KOH	
echo-MWCNTs	360	41	N/A	GCE	1 M KOH	*J. Am. Chem. Soc.* **2015**, *137*, 2901

ONPPGC/OCC	410	83	0.1	carbon cloth	1 M KOH	*Energy Environ. Sci.* **2016**, *9*, 1210
N-doped porous CC	360	98	8	carbon cloth	1 M KOH	*Energy Environ. Sci.* **2016**, *9*, 3411
Defective graphene	340	97	0.283	GCE	1 M KOH	*Adv. Mater.* **2016**, *28*, 9532
egg-CMS	N/A	59	~2	Ni foam	1 M KOH	*Adv. Energy Mater.* **2016**, *6*, 1600794
S,S'-CNT1000℃	350	95	0.284	pyrolytic graphite	1 M KOH	*Adv. Energy. Mater.* **2016**, *6*,1501966
P-doped graphene	330	62	0.2	GCE	1 M KOH	*Chem. Commun.* **2016**, *52*, 13008
Surface-oxidized carbon black	440	69	0.25	GCE	1 M KOH	*Chem. Commun.* **2016**, *52*, 6439
N-GRW	360	47	0.3	GCE	1 M KOH	*Sci. Adv.* **2016**, *2*, e1501122
N-HGS	400	52			1 M KOH	
N-GS	390	53			1 M KOH	
C_3N_4-CNT-CF	370	45	0.5	carbon fiber	1M KOH	*J. Mater. Chem. A.* **2016**, *4*, 12878.
BP-CNT	320	59.84	0.283	GCE	1M KOH	*Angew. Chem.* **2016**, *128*, 14053
C_3N_4/CNT	~300	N/A	0.204	GCE	1M KOH	*Angew. Chem. Int.*

						Ed. **2014**, *53*, 7281
N-graphene/CNT	420	N/A	0.425	GCE	0.1M KOH	*Angew. Chem. Int. Ed.* **2014**, *53*, 6496
Oxidized carbon cloth	477	82	N/A	carbon cloth	0.1M KOH	*Chem. Commun.* **2015**, *51*, 1616
C_3N_4/G	539	68.5	N/A	GCE	0.1M KOH	*ChemSusChem.* **2014**, *7*, 2125
GO-PANi31-FP	N/A	136	1	Ni foam	0.1M KOH	*Angew. Chem. Int. Ed.* **2016**, *55*, 13296
NCNF-1000	610	274	0.1	GCE	0.1M KOH	*Adv. Mater.* **2016**, *28*, 3000
NGM	440	N/A	0.25	GCE	0.1M KOH	*Adv. Mater.* **2016**, *28*, 6845

Table S3. Comparison of selected state-of-the-art non-noble-metal OER electrocatalysts in alkaline solution

Catalyst	Overpotential at 10mA cm^{-2} (mV vs. RHE)	Tafel slope (mV dec^{-1})	Mass loading (mg cm^{-2})	Substrate	Electrolyte	Reference
PEMAc@CNTs90	298	52	0.3	GCE	1 M KOH	This work
Mn-Co oxyphosphide multi-shelled particle	320	52	0.25	GCE	1 M KOH	*Angew. Chem. Int. Ed.* DOI: 10.1002/anie.201611804
CoMnP nanoparticles	330	61	0.284	GCE	1 M KOH	*J. Am. Chem. Soc.* 2016, 138, 4006
$Co_2(\mu\text{-}OH)_2$(bbta)	292	88	1.13	Cu foil	1 M KOH	*J. Am. Chem. Soc.*

						2016, 138, 8336
CoMn LDH	324	43	0.14	GCE	1 M KOH	*J. Am. Chem. Soc.* 2014, 136, 16481
NiCo LDH	367	40	0.17	Carbon paper	1 M KOH	*Nano Lettles.* 2015, 15, 1421
CoCo LDH	393	59	0.07	GCE	1 M KOH	*Nat. Commun.* 2014, 5, 4477
CoO/N-doped graphene	340	71	0.708	GCE	1 M KOH	*Energy Environ. Sci.* 2014, 7, 609
Ni_2P nanoparticles	290	59	0.14	GCE	1 M KOH	*Energy Environ. Sci.* 2015, 8, 2347
$CoFe_2O_4$/C NRAs	240	45	1.03	Ni foam	1 M KOH	*Adv. Mater.* DOI: 10.1002/adma.201604437
$CoFe_2O_4$/C powders	310	61	N/A	Ni foam		
Co-P film	345	47	2.71	Cu foil	1 M KOH	*Angew. Chem. Int. Ed.* 2015, 54, 6251
$NiFeO_x$ film	>350	N/A	N/A	GCE	1 M KOH	*J. Am. Chem. Soc.* 2013, 135, 16977
$NiCo_2O_4$ nanowires	~370	60	0.3	Ti mesh	1 M KOH	*Adv. Energy Mater.* 2015, 5, 141203
CoNi nanosheets	450	56.8	N/A	GCE	1 M KOH	*Chem. Sci.* 2015, 6, 3572
NiFe nanosheets	550	114	N/A	GCE		
Co_3O_4/C nanowires	290	70	~0.2	Cu foil	0.1 M KOH	*J. Am.*

array	220	61	~0.2		1 M KOH	*Chem. Soc.* 2014, 136, 13925
$SrNb_{0.1}Co_{0.7}Fe_{0.2}O_{3-\delta}$ nanorod	389	61	N/A	GCE	0.1 M KOH	*Adv. Energy Mater.* DOI: 10.1002/aenm.201602122
	370	48	0.464	GCE	1 M KOH	
Co_3O_4/rm-GO	310	67	0.24	GCE	1 M KOH	*Nat. Mater.* 2011, 10, 780

Table S4. The OER performance of commercial RuO_2 catalysts in some previous reports

RuO_2 (mg cm^{-2})	Overpotential at 10mA cm^{-2} (mV vs. RHE)	Substrate	Electrolyte	Reference
0.3	294	GCE	1 M KOH	This work
0.153	293	GCE	1 M KOH	*Energy Environ. Sci.* **2017**, *10*, 893
0.404	322	GCE	1 M KOH	*Small.* DOI: 10.1002/smll.201701025
0.6	280	Carbon paper	1 M KOH	*Adv. Sustainable Syst.* DOI: 10.1002/adsu.201700020
0.204	310	GCE	1 M KOH	*Small.* DOI: 10.1002/smll.201700796

Reference

[S1] U. J. Kim, C. A. Furtado, X. M. Liu, G. G. Chen and P. C. Eklund, *J. Am. Chem. Soc.,* 2005, **127**, 15437.

[S2] K. Tohji, T. Goto, H. Takahashi, Y. Shinoda, N. Shimizu, B. Jeyadevan, I. Matsuoka, Y. Saito, A. Kasuya, T. Ohsuna and H. Hiraga, *Nature*, 1996, **383**, 679.

[S3] J. Ma and J. N. Wang, *Chem. Mater.,* 2008, **20**, 2895.

[S4] (a) X. H. Chen, C. S. Chen, Q. Chen, F. Q. Cheng, G. Zhang and Z. Z. Chen, *Mater. Lett.,* 2002, **57**, 734. (b) V. Datsyuk, M. Kalyva, K. Papagelis, J. Parthenios, D. Tasis, A. Siokou, I. Kallitsis and C. Galiotis, *Carbon,* 2008, **46**, 833.

[S5] T. Sekitani, Y. Noguchi, K. Hata, T. Fukushima, T. Aida and T. Someya, *Science*, 2008, **321**, 1468.

[S6] M. H. Yu, Y. F. Zhang, Y. X. Zeng, M. S. Balogun, K. C. Mai, Z. S. Zhang, X. H. Lu and Y. X. Tong, *Adv. Mater.*, 2014, **26**, 4724.

[S7] Y. F. Zhang, Y. H. Tan, K. Yang, Z. X. Wu, Z. S. Zhang, M. Q. Zhang and K. C. Mai, *J. Mater. Chem. A*, 2016, **4**, 10091.

[S8] Z. S. Zhang, Y. F. Zhang, K. Yang, K. Y. Yi, Z. H. Zhou, A. P. Huang, K. C. Mai and X. H. Lu, *J. Mater. Chem. A*, 2015, **3**, 1884.

[S9] Z. F. Yang, Z. G. Xue, Y. G. Liao, X. P. Zhou, J. Q. Zhou, J. T. Zhu and X. L. Xie, *Langmuir.,* 2013, **29**, 3757.

[S10] D. Li, H. Baydoun, C. N. Verani and S. L. Brock, *J. Am. Chem. Soc.*, 2016, **138**, 4006.

[S11] Y. M. Jiang, X. Li, T. X. Wang and C. M. Wang, *Nanoscale.,* 2016, **8**, 9667.

[S12] X. Y. Lu, W. L. Yim, B. H. R. Suryanto and C. Zhao, *J. Am. Chem. Soc.,* 2015, **137**, 2901.

[S13] C. C. L. McCrory, S. Jung, J. C. Peters and T. F. Jaramillo, *J. Am. Chem. Soc.,* 2013, **135**, 16977.

[S14] (a) C. C. L. McCrory, S. Jung, I. M. Ferrer, S. M. Chatman, J. C. Peters and T. F. Jaramillo, *J. Am. Chem. Soc.,* 2015, **137**, 4347; (b) S. C. Huang, Y. Y. Meng, S. M. He, A. Goswami, Q. L. Wu, J. H. Li, S. F. Tong, T. Asefa and M. M. Wu, *Adv. Funct. Mater.,* DOI: 10.1002/adfm. 201606585; (c) T. A. Centeno and F. Stoeckli, *J. Power Sources.,* 2006, **154**, 314; (d) S. Trasatti and O. A. Petrii, *Pure & Appl. Chem.,* 1991, **63**, 711.

[S15] H. B. Yang, J. W. Miao, S. F. Hung, J. Z. Chen, H. B. Tao, X. Z. Wang, L. P. Zhang, R. Chen, J. J. Gao, H. M. Chen, L. M. Dai and B. Liu, *Sci. Adv.,* 2016, 2: e1501122.

[S16] F. Song and X. L. Hu, *J. Am. Chem. Soc*., 2014, **136**, 16481.

[S17] M. S. Dresselhaus, A. Jorio, A. G. Souza Filho and R. Saito, *Phil. Trans. R. Soc. A*, 2010, **368**, 5355.

[S18] L. G. Cançado, A. Jorio, E. H. Martins Ferreira, F. Stavale, C. A. Achete, R. B. Capaz, M. V. O. Moutinho, A. Lombardo, T. S. Kulmala and A. C. Ferrari, *Nano Lett.*, 2011, **11**, 3190.

[S19] L. G. Zhou and S. Q. Shi, *App. Phys. Lett.*, 2003, **83**, 1222.

[S20] B. Delley, *J. Chem.Phys.,* 1990, **92**, 508.

[S21] B. Delley, *J. Chem.Phys.,* 2000, **113**, 7756.

[S22] J. P. Perdew, K. Burke and M. Ernzerhof, *Phys. Rev. Lett.,* 1996, **77**, 3865.

[S23] I. C. Man, H. Su, F. Calle-Vallejo, H. A. Hansen, J. I. Martínez, N. G. Inoglu, J. Kitchin, T. F. Jaramillo, J. K. Nørskov and J. Rossmeisl, *ChemCatChem.,* 2011, **3**, 1159.

[S24] Q. Chen, L. Dai, M. Gao, S. Huang and A. Mau, *J. Phys. Chem. B.,* 2001, **105**, 618.

[S25] K. M. Lee, L. Li and L. Dai, *J. Am. Chem. Soc.,* 2005, **127**, 4122.

[S26] H. Li, T. Xu, C. Wang, J. Chen, H. Zhou and H. Liu, *Diam. Relat. Mater.,* 2006, **15**, 1228.

[S27] S. Y. Wang, D. S. Yu and L. M. Dai, *J. Am. Chem. Soc.,* 2011, **133**, 5182.

[S28] K. L. Lu, R. M. Lago, Y. K. Chen, M. L. H. Green, P. J. F. Harris and S. C. Tsang, *Carbon*, 1996, **34**, 814.

[S29] K. Mukhopadhyay, C. D. Dwivedi and G. N. Mathur, *Carbon*, 2002, **40**, 1369.

[S30] T. Mason and D. Peters, Practical Sonochemistry, Woodhead Publishing Limited, Cambridge, 2nd Edition, 2002.

[S31] H. J. Shin, S. M. Kim, S. M. Yoon, A. Benayad, K. K. Kim, S. J. Kim, H. K. Park, J. Y. Choi and Y. H. Lee, *J. Am. Chem. Soc.,* 2008, **130**, 2062.

[S32] H. Xu, X. Wang, Y. Zhang and S. Liu, *Chem. Mater.,* 2006, **18**, 2929.

[S33] Y. W. Liu, X. M. Hua, C. Xiao, T. F. Zhou, P. C. Huang, Z. P Guo, B. C. Pan and Y. Xie, *J. Am. Chem. Soc.,* 2016, **138**, 5087.

[S34] M. M. Fernández, R. M. Wagterveld, S. Ahualli, F. Liu, A. V. Delgado and H. V. M. Hamelers, *J. Power Sources*, 2016, **302**, 387.

[S35] Y. Lauw, M. D. Horne, T. Rodopoulos, A. Nelson and F. A. M. Leermakers, *J. Phys. Chem. B*, 2010, **114**, 11149.

[S36] A. G. Pandolfo and A. F. Hollenkamp, *J. Power Sources*, 2006, **157**, 11.

[S37] L. Wei and G. Yushin, *Nano Energy*, 2012, **1**, 552.

[S38] M. D. Merrill and R. C. Dougherty, *J. Phys. Chem. C,* 2008, **112**, 3655.

[S39] A. V. Narlikar and Y. Y. Fu, Eds. Oxford Handbook of Nanoscience and Technology: Frontiers and Advances, Oxford Univ. Press, Oxford, 2009.

[S40] Y. Jia, L. Z. Zhang, A. J. Du, G. P. Gao, J. Chen, X. C. Yan, C. L. Brown and X. D. Yao, *Adv. Mater.,* 2016, **28**, 9532.

[S41] C. Tang, H. F. Wang, X. Chen, B. Q. Li, T. Z. Hou, B. S. Zhang, Q. Zhang, M. M. Titirici and F. Wei, *Adv. Mater.* 2016, **28**, 6845.

[S42] G. Zhang, G. C. Wang, Y. Liu, H. J. Liu, J. H.Qu and J. H. Li, *J. Am. Chem. Soc.*, 2016, **138**, 14686.

[S43] Y. Y. Meng, D. Voiry, A. Goswami, X. X. Zou, X. X. Huang, M. Chhowalla, Z. W. Liu and T. Asefa, *J. Am. Chem. Soc.*, 2014, **136**, 13554.

[S44] A. T. Swesi, J. Masud and M. Nath, *Energy Environ. Sci.*, 2016, **9**, 1771.

[S45] Y. Qiu, L. Xin and W. Z. Li, *Langmuir*, 2014, **30**, 7893.

[S46] R. Sen, B. Zhao, D. Perea, M. E. Itkis, H. Hu, J. Love, E. Bekyarova and R. C. Haddon, *Nano Letters*, 2004, **4**, 459.